Influence of texture and transformation strain on the superelastic performance of a new Ti–20Zr–3Mo–3Sn alloy

J.J. Gao, I. Thibon, D. Laillé, Philippe Castany, T. Gloriant

Influence of texture and transformation strain on the superelastic performance of a new Ti-20Zr-3Mo-3Sn alloy

J.J. Gao, I. Thibon, D. Laillé, P. Castany, T. Gloriant*

Univ Rennes, INSA Rennes, CNRS, ISCR UMR 6226, 35000 Rennes, France

*Corresponding author: e-mail: Thierry.Gloriant@insa-rennes.fr

Abstract:

In this work, the superelastic behavior of a new metastable β Ti-20Zr-3Mo-3Sn (at.%) biomedical alloy displaying stress-induced α" martensitic transformation (SIM) was investigated by cyclic tensile tests, electron back-scattered diffraction (EBSD) and in situ synchrotron X-ray diffraction (SXRD) for 3 different solution treatment temperatures: 700°C, 800°C and 900°C. The EBSD observations revealed that the Ti-20Zr-3Mo-3Sn alloy showed a strong dependence of the solution treatment temperatures on crystallographic texture. SXRD diffraction profiles acquired under cyclic loading/unloading tensile tests clearly illustrated the reversible SIM α" transformation. In addition, the lattice parameters of β and SIM α" phases were measured for each cycle in order to establish the evolution of lattice parameters during the deformation and to calculate the maximum transformation strain for any crystallographic direction. A high recovery strain of 3.5% was obtained by tensile test after a solution treatment at 700°C for 30 minutes. This high recovery strain is due to the fact that the maximum transformation strain is obtained along the tensile direction displaying the favorable $<011>_{\beta}\{100\}_{\beta}$ recrystallization texture. The performance of the Ti-20Zr-3Mo-3Sn alloy is discussed and compared with other superelastic alloys such as NiTi and (Ti-Nb)-based alloys.

Keywords: titanium alloys; superelasticity; martensitic transformation; texture; transformation strain

1. Introduction

Near equiatomic NiTi alloys are commonly used for the manufacture of biomedical devices such as orthodontic arches, orthopedic staples, endovascular stents… due to their high strength, good corrosion resistance and their high and useful superelastic effect which is required for such applications. However, Ni hypersensitivity still remains an issue in terms of biocompatibility [1] and superelastic Ni-free β-titanium alloys displaying stress-induced α" martensitic transformation (SIM) are now considered as the right alternative option for biomedical applications. Consequently, numerous superelastic (Ti-Nb)-based alloys have been widely developed, such as Ti–Nb–Al, Ti–Nb–Zr, Ti–Nb–Ta, Ti-Nb-O, Ti-Nb-N, Ti-Nb-Zr-Sn, Ti–Nb–Zr–Ta, Ti–Nb–Ta–Zr–O [2-14]. However, most of (Ti-Nb)-based alloys showed low recovery strain (less than 3.0%) compared to NiTi alloys (more than 8.0%). The poor recovery strain is attributed to the small transformation strain from body-centered cubic β phase (space group N^{o}229, Im-3m) to C-centered orthorhombic α" martensitic phase (space group N^{o}63, Cmcm) [9]. Recently, it was reported that hafnium [15] or zirconium [16, 17] can be effective alloying elements to improve the superelastic performance of Ni-free titanium-based alloys. Indeed, the substitution of niobium by zirconium allowed the control of the martensitic transformation start temperature in order to promote superelasticity at room temperature and a strain recovery as high as 7.0% could be reached in some optimized chemical compositions [17].

In this work, a new quaternary superelastic Ti-20Zr-3Mo-3Sn (at.%) alloy was designed with high zirconium content to replace niobium. Molybdenum was selected as beta stabilizing element and tin was used to suppress the ω phase formation [16]. Once elaborated, the alloy was investigated by cyclic tensile tests and characterized by electron back-scattered diffraction (EBSD) for 3 different solution treatment temperatures: 700°C, 800°C and 900°C with the objective to evaluate the influence of the recrystallization texture on its superelastic performance. On the other hand, in situ synchrotron X-ray diffraction (SXRD) characterizations on loading were conducted to

follow the deformation sequence and the evolution of the lattice parameters of both phases in order to calculate the maximum transformation strain. Indeed, it is well established that the superelastic recovery strain is attributed to the lattice transformation strain capacity between β and α" phases [2, 3, 16, 17]. Thus, an objective of this study is also to clarify the role of the chemical composition, and particularly the zirconium element, on the superelastic performance. Although a maximum recovery strain is required for efficient superelastic medical devices, minimum values must also be taken into consideration for a good functionality. Indeed, superelastic medical devices often present a complex geometry and it remains difficult to control the texture during their fabrication. As this point is rarely addressed in literature, the minimum recovery strain is also investigated in the present study and inverse pole figures of transformation strains for all crystallographic orientations will be calculated for comparison with other superelastic alloys such as NiTi and (Ti-Nb)-based alloys.

2. Material and methods

2.1. Alloy synthesis and sample preparation

The Ti-20Zr-3Mo-3Sn alloy (at.%) was synthesized by cold crucible levitation melting (CCLM) technique under argon atmosphere. For this synthesis, pure raw metals included 99.95% pure titanium, 99.078% pure zirconium, 99.9% pure molybdenum and 99.99% pure tin were used. After melting, ingot was homogenized at 950°C for 1200 min under high vacuum (10^{-7} mbar), followed by water quenching. Then, the ingot was cold rolled until 95% reduction rate in thickness. Dog-bone tensile specimens were machined from the cold-rolled sheets with normalized shape: 3 mm width, 0.5 mm in thickness and a gage length of 15 mm. In order to restore a fully recrystallized microstructure from the cold-rolled state, the tensile specimens were finally solution-treated under high vacuum (10^{-7} mbar) at 3 different temperatures (T=700, 800, and 900°C) for 30 minutes in the β-phase domain followed

by a water quenching in order to retain the β-phase in its metastable state.

In the present study, the 3 solution treatment temperatures were chosen after the determination of the β transus temperature of the alloy, which was obtained by measuring the electrical resistivity variation upon temperature. Indeed, electrical resistivity, which is very sensitive to microstructural changes, is an effective thermal analysis technique for detecting such beta transus temperature [18, 19]. The resistivity measurements were performed on a lamella sample by using the four-probe method under high vacuum (10^{-7} mbar) between room temperature and 950°C and with a heating/cooling rate of 5°C/min. For the measurements, serial electrical circuit set-up composed of the sample (with resistivity ρ), a reference resistor (2 ohm) and a d.c. source was used. If we neglect the thermal expansion of the sample, variation of the electrical resistivity ratio ρ/ρ_0 (ρ_0: initial resistivity at room temperature) can be plotted as a function of temperature. Fig.1 shows the typical resistivity curve usually observed from metastable β-Ti alloys, which was obtained between 400°C and 900°C during a heating/cooling cycle in the present study. On this curve, the red part corresponds to the heating and the blue part to the cooling. The detection of the β transus in titanium alloys by resistivity measurements corresponds to the temperature from which the heating and cooling measurements are superimposed [18]. As shown on this resistivity curve, the β transus temperature was measured to be 690°C for the studied Ti-20Zr-3Mo-3Sn alloy.

2.2. Tensile tests and microstructural analysis methods

Tensile tests with the strain rate of 10^{-4} s^{-1} were performed to evaluate the mechanical properties of the different samples. The tensile direction was chosen parallel to the cold rolling direction (RD). In this study, cyclic loading-unloading tensile tests were particularly employed in order to characterize the superelastic behavior of the Ti-20Zr-3Mo-3Sn alloy after the different solution treatments. For that, tensile stress is applied until the strain reaches 0.5% for the first cycle, and then the load is removed. The measurement is repeated through increasing the strain by 0.5%

steps upon loading for the same specimen. An extensometer was used to measure the strain of the specimens during these tests.

To characterize the microstructure after the different solution treatments, electron back-scattered diffraction (EBSD) analyses were conducted with a scanning electron microscope (Jeol JSM 7100F, SEM) equipped with an Oxford HKL EBSD system. Prior to the EBSD observations, all the specimens were mechanically mirror-polished by using several SiC papers with decreasing grid size and followed by colloidal silica suspension (particles size: 0.05 μm). In this work, the colloidal silica suspension was mixed with H_2O_2 solution to release stress due to polishing and reveal the microstructure.

In situ synchrotron X-ray diffraction (SXRD) analyses under cyclic tensile tests were conducted in this study. SXRD experiments were carried out at the ID-22 high resolution powder diffraction beamline of the European Synchrotron Radiation Facility (ESRF, Grenoble, France) with a 1 mm^2 X-ray beam size and a 0.35453630 Å wavelength radiation. The in situ cyclic tensile tests (at the rate of 10^{-4} s^{-1}) under synchrotron radiation were performed with increments of 0.5% until 5.0% of strain and then increased by 1.0% until 6.0% of strain during each loading and unloading condition. A nine-channel detector was used to collect transmitted diffracted beams and all the SXRD profiles between $2\theta=6°$ and $2\theta=20°$ were obtained for each cycle.

3. Results

3.1. Tensile tests

Fig.2 displays the engineering stress-strain curves, which were obtained from cyclic tensile tests for specimens subjected to three different solid solution treatments in the β-phase domain: 700°C for 30 min (ST-700-30, Fig.2.a), 800°C for 30 min (ST-800-30, Fig.2.b) and 900°C for 30 min (ST-900-30, Fig.2.c). In these tensile curves, the presence of hysteresis between loading and unloading is due to the superelastic property of the alloy in which reversible SIM transformation between β and α" phases occurs. Up to four cycles, they all show a very good superelastic

behavior performance, the recoverable strain can return back to origin totally. With increasing applied strain, residual strain appears meaning that the inverse martensitic transformation is not complete. In this figure, the cycle showing the maximum recovered strain is marked in bold for each sample. The maximum recovery strain is then measured to be 3.5%, 2.7% and 2.5% for ST-700-30, ST-800-30 and ST-900-30, respectively.

3.2. Electron back-scattered diffraction characterizations (EBSD)

Analyses by EBSD were carried out in this study to characterize the recrystallization texture induced by the different solution treatments. Typical EBSD inverse pole figure (IPF) maps obtained from the alloy subjected to the three different solution treatments (ST-700-30, ST-800-30 and ST-900-30) are shown in Fig.3.a, 3.b and 3.c, respectively. The color code corresponding to the crystallographic grain orientation is shown in Fig.3.d (the Rolling Direction is represented). All the samples show a typical equiaxed β-grain microstructure. A predominant green color is observed in the Fig.3.a, indicating a dominant of $\{hkl\}_{\beta}<101>_{\beta}$ texture when the alloy is solution-treated at 700°C. However, red-colored grains are dominating in Fig.3.b, demonstrating that $\{hkl\}_{\beta}<001>_{\beta}$ is the preferential orientation when the alloy is solution-treated at 800°C. On the other hand, a random distribution of color is obtained in Fig.3.c when the alloy is solution-treated at 900°C. Consequently, it is worth noting that the temperature of the solution treatment is on great influence on the crystallographic orientation. This observation is not surprising since it is well known that the cold-rolled rate and the recrystallization temperature greatly influence the texture in many metallic alloys [20]. In order to determine more precisely the recrystallized textures, the ODF (orientation distribution function) have been calculated for each sample (available as supplementary materials) and inverse pole figures of textures are presented in Fig.4 for each solution treatment. In this figure, RD and ND correspond to the rolling direction (parallel to the tensile direction) and the normal direction, respectively. For the ST-700-30 sample (Fig.4.a), a dominant $<011>_{\beta}\{100\}_{\beta}$ texture is evidenced but a $<111>_{\beta}\{213\}_{\beta}$ texture component is also

observed to a lesser extent. For the ST-800-30 specimen, it is shown a strong $<100>_{\beta}\{011\}_{\beta}$ texture (Fig.4.b). For the last one, in the case of the ST-900-30 specimen, a principal $<113>_{\beta}\{110\}_{\beta}$ texture and a slightly $<110>_{\beta}\{111\}_{\beta}$ textures are obtained (Fig.4.c).

3.3. In situ synchrotron X-ray diffraction (SXRD)

In order to evidence the SIM transformation occurring in the Ti-20Zr-3Mo-3Sn alloy, in situ SXRD under cyclic loading/unloading tensile test has been conducted on the ST-700-30 specimen. Fig.5 displays the initial SXRD profile (in black), the SXRD profile under loading maintained at 6.0% of strain (in red) and the SXRD profile after unloading (in blue). Prior to deformation, the initial SXRD profile shows the typical diffraction peaks: $(110)_{\beta}$, $(002)_{\beta}$, $(112)_{\beta}$, $(202)_{\beta}$, $(013)_{\beta}$ of the cubic β phase (black profile). After being deformed to 6.0% strain, only the diffraction peaks related to the orthorhombic α" martensitic phase are detected (red profile): $(020)_{\alpha''}$, $(002)_{\alpha''}$, $(021)_{\alpha''}$, $(022)_{\alpha''}$, $(113)_{\alpha''}$, etc.… meaning that the alloy is fully martensitic under this 6.0% of strain. When the load is released, both α" and β peaks are detected. In order to characterize more precisely the martensitic phase transformation, it is presented in Fig.6 the evolution of the most intense β phase peak and α" martensitic phase peaks within the restricted 7.6 - 9.4° angle range during the entire cyclic tensile test from 0 to 6.0% strain on loading (Fig.6.a) and after unloading (Fig.6.b). One can notice that the $(110)_{\beta}$ peak is slightly shifted to the left at the beginning of the deformation (up to 1.5% of strain), compared to its initial position. On the other hand, the $(002)_{\alpha''}$, $(020)_{\alpha''}$, $(021)_{\alpha''}$ martensitic peaks start to be detected at 1.5% of strain, which is in good agreement with the cyclic tensile curve. When the strain increases, the intensity of detected martensitic peaks increases progressively to the detriment of the β phase $(110)_{\beta}$ peak. After unloading from the lowest 4.0% of strain (Fig.6.b), the main detected peak seems to be the $(110)_{\beta}$ peak of the β phase but in fact, a slight $(002)_{\alpha''}$ martensitic peak is also observed in superimposition. Consequently, the reversible stress-induced martensitic transformation is thus clearly evidenced by these in situ SXRD experiments. The other peaks of the martensitic phase can also be observed

after unloading but only when the alloy was deformed at a strain superior to 4.5%.

For both parent β and martensitic α" phases, the shift of peaks indicates a variation of the lattice parameters. Thus, the evolution of lattice parameters of β phase (a_β) and α" martensite phase ($a_{\alpha"}$, $b_{\alpha"}$, $c_{\alpha"}$) determined from the whole SXRD profiles is plotted in Fig.7 as a function of the applied strain on loading. Before deformation, the lattice parameter of the β phase is measured to be a_β=0.3332 nm. When the strain increases, the β phase is elastically deformed and its a_β parameter raises a maximum value of 0.3365 nm at 1.5% of strain and remains constant for higher strain values. Concerning the stress-induced α" martensitic phase, which starts to be detected at 1.5% of strain, its $a_{\alpha"}$ lattice parameter remains more or less constant in the studying strain range but its $b_{\alpha"}$ and $c_{\alpha"}$ parameters continually increase. Indeed the $b_{\alpha"}$ lattice parameter increases from 0.5080 nm (at 2.0% of strain) to a constant value of 0.5104 nm while the $c_{\alpha"}$ parameter increases from 0.4740 nm to 0.4770 nm at 5.0% of strain, where the plastic deformation begins. Consequently, the deformation sequence of the Ti-20Zr-3Mo-3Sn alloy under tensile load can be divided in three parts as shown in Fig.7: the β phase is first deformed elastically until 1.5% of applied strain (I), secondly, the SIM transformation occurred from 1.5% to 5.0% of strain together with its elastic deformation (II), and finally, the plastic deformation occurred from 5.0% of strain (III).

4. Discussion

Recently, new (Ti-Zr)-based superelastic alloys have demonstrated a remarkably recovery strain, which is due to the fact that a strong $<101>_\beta$ type crystallographic texture was observed parallel to the tensile direction [16, 17]. Thus, around 7.0% of recovery strain was obtained by tensile test for the Ti-24Zr-10Nb-2Sn alloy composition (at.%) heat treated at 1173 K for 1.8ks. It is worth noting that this remarkable large elastic recovery value is more than three times that of other Ni-free (Ti-Nb)-based superelastic alloys [17], which constitutes an excellent result since it becomes comparable with those obtained with the commonly superelastic NiTi alloy

used for biomedical applications [21]. In superelastic alloys, the crystallographic texture was shown to be a very important parameter influencing the recovery strain. However, the transformation strain capability between β and α" phases must also be taken into account in order to optimize the superelastic recovery performance. Indeed, the transformation strain does not only depend on the orientation of the β grains but also on the lattice parameters of both β and α" phases, which depend on the chemical composition of the alloy.

From the superelastic titanium alloys, there are 6 equivalent correspondence variants that can be formed when a cubic crystal of β phase transforms into an orthorhombic α" martensite crystal with respect of the classical $\{110\}_{\beta}\|(001)_{\alpha''}$ and $<111>_{\beta}\|[110]_{\alpha''}$ orientation relationships. But when the martensite is stress-induced, a variant selection operates in order to form only the variants that can accommodate the imposed deformation. It is thus commonly assumed that the variant that is activated and growth is the one that gives the maximum transformation strain in each grain. According to that, the transformation strain induced by the lattice distortion due to the martensitic transformation from the β cubic phase to the orthorhombic α" phase can be calculated for any direction as a function of lattice parameters of both phases [2]. As the maximum transformation strains depend on the lattice parameters of each phase, one can easily calculate them for the present Ti-20Zr-3Mo-3Sn alloy for which the lattice parameters for both β and α" phases were evaluated by SXRD in this study. Table 1 reports these lattice parameter values for the Ti-20Zr-3Mo-3Sn alloy of the present study and those obtained on a typical (Ti-Nb)-based superelastic alloy (the Ti-24Nb-4Zr-8Sn alloy composition in wt.%) elaborated and characterized by our group with an identical approach [22, 23] for comparison. For example, the maximum transformation strain values, ε_{hkl} (given in %), that correspond to the three principal crystallographic directions of the body-centered cubic β phase can be calculated as follow [2, 24, 25]:

$$\varepsilon_{110} = \frac{b_{\alpha''} - \sqrt{2}a_{\beta}}{\sqrt{2}a_{\beta}} \times 100 \quad (1)$$

$$\varepsilon_{001} = \frac{\sqrt{b_{\alpha''}^2 + c_{\alpha''}^2} - 2a_\beta}{2a_\beta} \times 100 \quad (2)$$

$$\varepsilon_{111} = \frac{\sqrt{a_{\alpha''}^2 + b_{\alpha''}^2} - \sqrt{3}a_\beta}{\sqrt{3}a_\beta} \times 100 \quad (3)$$

Where a_β corresponds to the lattice parameter of the β phase and $a_{\alpha''}$, $b_{\alpha''}$, $c_{\alpha''}$ correspond to the lattice parameters of the α" phase.

These calculated values for both Ti-20Zr-3Mo-3Sn and Ti-24Nb-4Zr-8Sn alloys are reported in table 1 and it can be seen that the highest transformation strain is always obtained for the $<101>_\beta$ direction. Indeed, the theoretical maximum transformation strain, ε_{110}, that can be expected is thus 7.3% and 3.6% for the Ti-20Zr-3Mo-3Sn and Ti-24Nb-4Zr-8Sn alloys, respectively. Consequently, it is not surprising to obtain the best recovery strain when the present alloy is treated at 700°C since the principal texture observed, which is $<101>_\beta$ direction, is aligned to the tensile direction, unlike those obtained for the other treatments (800°C and 900°C).

These calculated values represent a similar tendency with the experimental superelastic recovery strains that were measured for each alloy to be 3.50% and 2.25%, respectively. Consequently, the zirconium element, instead of niobium, seems to play an important role since the $b_{\alpha''}$ lattice parameter is much higher in the case of the Ti-20Zr-3Mo-3Sn alloy with the consequence that this alloy presents a larger stain recovery compared to the Ti-24Nb-4Zr-8Sn alloy.

As previously mentioned, the calculated maximum transformation strain induced by the lattice distortion between β and α" can be generalized for all crystallographic directions [2, 24, 25]. Indeed, the deformation in any x vector of the β phase is transformed to $x'^{(Vi)}$ through the martensite α" transformation by:

$$x'^{(Vi)} = T^{(Vi)}.x \quad (4)$$

Where $T^{(Vi)}$ represents the lattice distortion matrix expressed in the coordinates of the β phase for each variants Vi. In the cubic to orthorhombic transformation, there are 6 equivalent correspondence variants of martensite (i=1 to 6), therefore there are 6 lattice distortion matrices to take into consideration [24].

Hence the maximum transformation strain, $\varepsilon_{hkl}^{(Vi)}$, due to the lattice distortion for each variant and for any direction can be calculated as follows:

$$\varepsilon_{hkl}^{(Vi)} = \frac{|x'^{(Vi)}| - |x|}{|x|} \quad (5)$$

From this calculation using the lattice parameters determined by SXRD (Table 1), inverse pole figure distribution of maximum transformation strains (IPF-TS) can be drawn as shown in Fig.8. This figure presents the IPF-TS for the Ti-20Zr-3Mo-3Sn (top) and Ti-24Nb-4Zr-8Sn (bottom) alloys, respectively. As shown, the maximum transformation strain is obtained for the $<101>_\beta$ direction and the minimum for the $<111>_\beta$ direction (2.5% and 0.6% for the Ti-20Zr-3Mo-3Sn and the Ti-24Nb-4Zr-8Sn alloys, respectively). Thus, the fact to substitute niobium by a relatively large amount of zirconium is very judicious because this later can modify significantly the lattice parameters implying a large difference between a_β and $b_{\alpha''}$, which must be obtained together with a pure $<011>_\beta\{100\}_\beta$ recrystallization texture in order to promote the highest superelastic recovery. Of course, calculated transformation strains and experimental recovery strains cannot be compared directly. First because the pure $<011>_\beta\{100\}_\beta$ recrystallization texture was not obtained, even in the case of the most favorable thermal treatment (700°C) where a $<111>_\beta\{213\}_\beta$ component is also obtained, and secondly, because the calculated maximum transformation strains don't take into account the presence of grain boundaries and grain sizes or other defects, such as the formation dislocations that can be on great influence on the real recovery strain [26]. However, comparable tendency is observed and the higher is the calculated transformation strain, the higher is the experimental recovery strain.

Another point that deserves to be discussed concerns the minimum values obtained. Although a maximum recovery strain is required for efficient superelastic medical devices, minimum values must also be taken into consideration for a good functionality. Indeed, superelastic medical devices often present a complex geometry and it remains difficult to control the texture during their fabrication. Consequently, parts of the device can present unfavorable texture leading to low recovery strain, which represents a weakness for a considered device. It is then demonstrated through

this study the advantage of using zirconium instead of niobium as principal alloying element due to the fact that the minimum value of transformation strain obtained for the Ti-20Zr-3Mo-3Sn alloy (2.5%) is 4 times higher than the minimum value of transformation strain obtained for the Ti-24Nb-4Zr-8Sn alloy (0.6%, which is very low). On the other hand, calculated transformation strains for the B2-B19' martensitic transformation in NiTi alloys can be found in literature for comparison [27, 28]. Although NiTi alloys can display a very high maximum transformation strain value in tension reaching more than 10.0% in the most favorable $<355>_{B2}$ crystallographic direction, the minimum calculated value is only 2.7% in the most unfavorable $<001>_{B2}$ direction, which is comparable with the minimum value obtained with the alloy of the present study (2.5%). Consequently, this new Ti-20Zr-3Mo-3Sn alloy composition is potentially very interesting and competitive to replace NiTi alloy for the manufacture of superelastic medical devices as new Ni-free alloy.

5. Conclusions

As a summary, a newly developed Ti-20Zr-3Mo-3Sn (at.%) superelastic alloy for biomedical applications was designed and elaborated in this study. In order to investigate the superelastic performance of this alloy, cyclic tensile tests, EBSD and in situ SXRD characterizations have been conducted after 3 different solution treatment temperatures: 700°C, 800°C and 900°C.

The EBSD observations revealed that the Ti-20Zr-3Mo-3Sn β-grain microstructure showed a strong dependence of the solution treatment temperature on crystallographic texture and three different textures were obtained. By in situ SXRD, the typical diffraction peaks of the β and SIM α" phases during loading/unloading were clearly observed and the reversible transformation between the β phase and the SIM α" phase was evidenced. On the other hand, the lattice parameters of β and SIM α" phases were measured for each cycle and their evolutions during the deformation were established. From these measurements, the maximum transformation strain for any crystallographic direction was evaluated and inverse pole figures of maximum

transformation strain (IPF-TS) were established for the present Ti-20Zr-3Mo-3Sn alloy and for the Ti-24Nb-4Zr-8Sn alloy, which was characterized in a previous work by the same approach. By comparing the IPF-TS of the two alloys, it was showed that the Ti-20Zr-3Mo-3Sn alloy presents much higher maximum transformation strain values than Ti-24Nb-4Zr-8Sn alloy whatever the crystallographic orientation. Finally, the highest recovery strain obtained with the Ti-20Zr-3Mo-3Sn alloy (3.5%) can then be explained by the high zirconium content that modifies significantly the lattice parameters implying a large difference between a_β and $b_{\alpha''}$, which must be obtained together with a pure $<011>_\beta\{100\}_\beta$ recrystallization texture in order to promote the highest strain recovery.

Acknowledgment

J.J. Gao acknowledges the China Scholarship Council (CSC) for his Ph.D financial support (No. 2016-6329). The authors also acknowledge the SCANMAT platform of the University of Rennes for providing access to SEM facilities.

References

[1] D.J. Wever, A.G. Veldhuizen, M.M. Sanders, J.M. Schakenraad, J.R. Van Horn, Cytotoxic, allergic and genotoxic activity of a nickel-titanium alloy, Biomater. 18 (1997) 1115-1120.

[2] H.Y. Kim, Y. Ikehara, J.I. Kim, H. Hosoda, S. Miyazaki, Martensitic transformation, shape memory effect and superelasticity of Ti–Nb binary alloys, Acta Mater. 54 (2006) 2419-2429.

[3] T. Inamura, Y. Fukui, H. Hosoda, K. Wakashima, S. Miyazaki, Relationship between texture and macroscopic transformation strain in severely cold-rolled Ti-Nb-Al superelastic alloy, Mater. Trans. 45 (2004) 1083-1089.

[4] F. Sun, Y.L. Hao, S. Nowak, T. Gloriant, P. Laheurte, F. Prima, A thermo-mechanical treatment to improve the superelastic performances of

biomedical Ti–26Nb and Ti–20Nb–6Zr (at.%) alloys, J. Mech. Behav. Biomed. Mater. 4 (2011) 1864-1872.

[5] H. Hosoda, Y. Kinoshita, Y. Fukui, T. Inamura, K. Wakashima, H.Y. Kim, S. Miyazaki, Effects of short time heat treatment on superelastic properties of a Ti–Nb–Al biomedical shape memory alloy, Mater. Sci. Eng. A 438 (2006) 870-874.

[6] J.I. Kim, H.Y. Kim, T. Inamura, H. Hosoda, S. Miyazaki, Shape memory characteristics of Ti–22Nb–(2–8) Zr (at.%) biomedical alloys, Mater. Sci. Eng. A 403 (2005) 334-339.

[7] H.Y. Kim, T. Sasaki, K. Okutsu, J.I. Kim, T. Inamura, H. Hosoda, S. Miyazaki, Texture and shape memory behavior of Ti–22Nb–6Ta alloy, Acta Mater. 54 (2006) 423-433.

[8] A. Ramarolahy, P. Castany, F. Prima, P. Laheurte, I. Péron, T. Gloriant, Microstructure and mechanical behavior of superelastic Ti–24Nb–0.5 O and Ti–24Nb–0.5N biomedical alloys, J. Mech. Behav. Biomed. Mater. 9 (2012) 83-90.

[9] P. Castany, A. Ramarolahy, F. Prima, P. Laheurte, C. Curfs, T. Gloriant, In situ synchrotron X-ray diffraction study of the martensitic transformation in superelastic Ti-24Nb-0.5 N and Ti-24Nb-0.5 O alloys, Acta Mater. 88 (2015) 102-111.

[10] Y.L. Hao, Z.B. Zhang, S.J. Li, R. Yang, Microstructure and mechanical behavior of a Ti–24Nb–4Zr–8Sn alloy processed by warm swaging and warm rolling, Acta Mater. 60 (2012) 2169-2177.

[11] Y.L. Hao, S.J. Li, S.Y. Sun, C.Y. Zheng, R. Yang, Elastic deformation behaviour of Ti–24Nb–4Zr–7.9 Sn for biomedical applications, Acta Biomater. 3 (2007) 277-286.

[12] M. Tahara, H.Y. Kim, H. Hosoda, T. Nam, S. Miyazaki, Effect of nitrogen addition and annealing temperature on superelastic properties of Ti–Nb–Zr–Ta alloys, Mater. Sci. Eng. A 527 (2010) 6844-6852.

[13] M. Besse, P. Castany, T. Gloriant, Mechanisms of deformation in gum metal

TNTZ-O and TNTZ titanium alloys: A comparative study on the oxygen influence, Acta Mater. 59 (2011) 5982–5988.

[14] Y. Yang, G.P. Li, G.M. Cheng, Y.L. Li, K. Yang, Multiple deformation mechanisms of Ti–22.4Nb–0.73Ta–2.0Zr–1.34O alloy, Appl. Phys. Lett. 94 (2009) 061901.

[15] M.F. Ijaz, D. Laillé, L. Héraud, D.-M. Gordin, P. Castany, T. Gloriant, Design of a novel superelastic Ti-23Hf-3Mo-4Sn biomedical alloy combining low modulus, high strength and large recovery strain, Mater. Lett. 177 (2016) 39-41.

[16] M.F. Ijaz, H.Y. Kim, H. Hosoda, S. Miyazaki, Superelastic properties of biomedical (Ti–Zr)–Mo–Sn alloys, Mater. Sci. Eng. C 48 (2015) 11-20.

[17] L.L. Pavón, H.Y. Kim, H. Hosoda, S. Miyazaki, Effect of Nb content and heat treatment temperature on superelastic properties of Ti–24Zr–(8–12)Nb–2Sn alloys, Scripta Mater. 95 (2015) 46-49.

[18] D.-M. Gordin, E. Delvat, R. Chelariu, G. Ungureanu, M. Besse, D. Laillé, T. Gloriant, Characterization of Ti-Ta Alloys Synthesized by Cold Crucible Levitation Melting, Adv. Eng. Mater. 10 (2008) 714-719.

[19] F. Sun, F. Prima, T. Gloriant, High-strength nanostructured Ti–12Mo alloy from ductile metastable beta state precursor, Mater. Sci. Eng. A 527 (2010) 4262-4269.

[20] R. D. Doherty, Recrystallization and texture, Prog. Mater. Sci. 42 (1997) 39-58.

[21] L. Héraud, P. Castany, D. Lailllé, T. Gloriant, In Situ Synchrotron X-ray Diffraction of the Martensitic Transformation in Superelastic Ti-27Nb and NiTi Alloys: A Comparative Study, Mater. Today: Proc. 2 (2015) S917-S920.

[22] Y. Yang, P. Castany, M. Cornen, F. Prima, S.J. Li, Y.L. Hao, T. Gloriant, Characterization of the martensitic transformation in the superelastic Ti–24Nb–4Zr–8Sn alloy by in situ synchrotron X-ray diffraction and dynamic mechanical analysis, Acta Mater. 88 (2015) 25-33.

[23] Y. Yang, P. Castany, M. Cornen, I. Thibon, F. Prima, T. Gloriant, Texture

investigation of the superelastic Ti–24Nb–4Zr–8Sn alloy, J. Alloys Compd. 591 (2014) 85-90.

[24] M. Tahara, H.Y. Kim, T. Inamura, H. Hosoda, S. Miyazaki, Lattice modulation and superelasticity in oxygen-added β-Ti alloys, Acta Mater. 59 (2011) 6208-6218.

[25] E. Bertrand, P. Castany, Y. Yang, E. Menou, T. Gloriant, Deformation twinning in the full-α ″martensitic Ti–25Ta–20Nb shape memory alloy, Acta Mater. 105 (2016) 94-103.

[26] F. Sun, S. Nowak, T. Gloriant, P. Laheurte, A. Eberhardt, F. Prima, Influence of a short thermal treatment on the superelastic properties of a titanium-based alloy, Scripta Mater. 63 (2010) 1053-1056.

[27] L. Isola, P. La Roca, C. Sobrero, V. Fuster, P. Vermaut, J. Malarría, Martensitic transformation strain and stability of Ni_{50-x}–Ti_{50}–Co_x (x= 3, 4) strips obtained by twin-roll casting and standard processing techniques, Mater. Des. 107 (2016) 511-519.

[28] S.C. Mao, J.F. Luo, Z. Zhang, M.H. Wu, Y. Liu, X.D. Han, EBSD studies of the stress-induced B2–B19′ martensitic transformation in NiTi tubes under uniaxial tension and compression, Acta Mater. 58 (2010) 3357-3366.

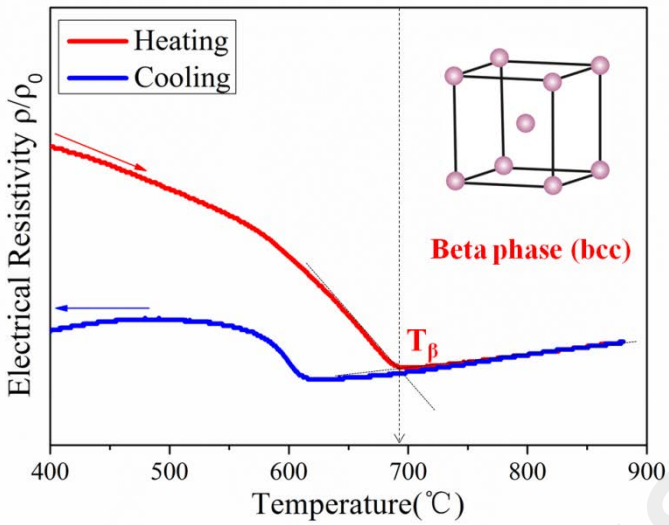

Fig. 1. Electrical resistivity curve of the Ti-20Zr-3Mo-3Sn alloy (heating and cooling cycle).

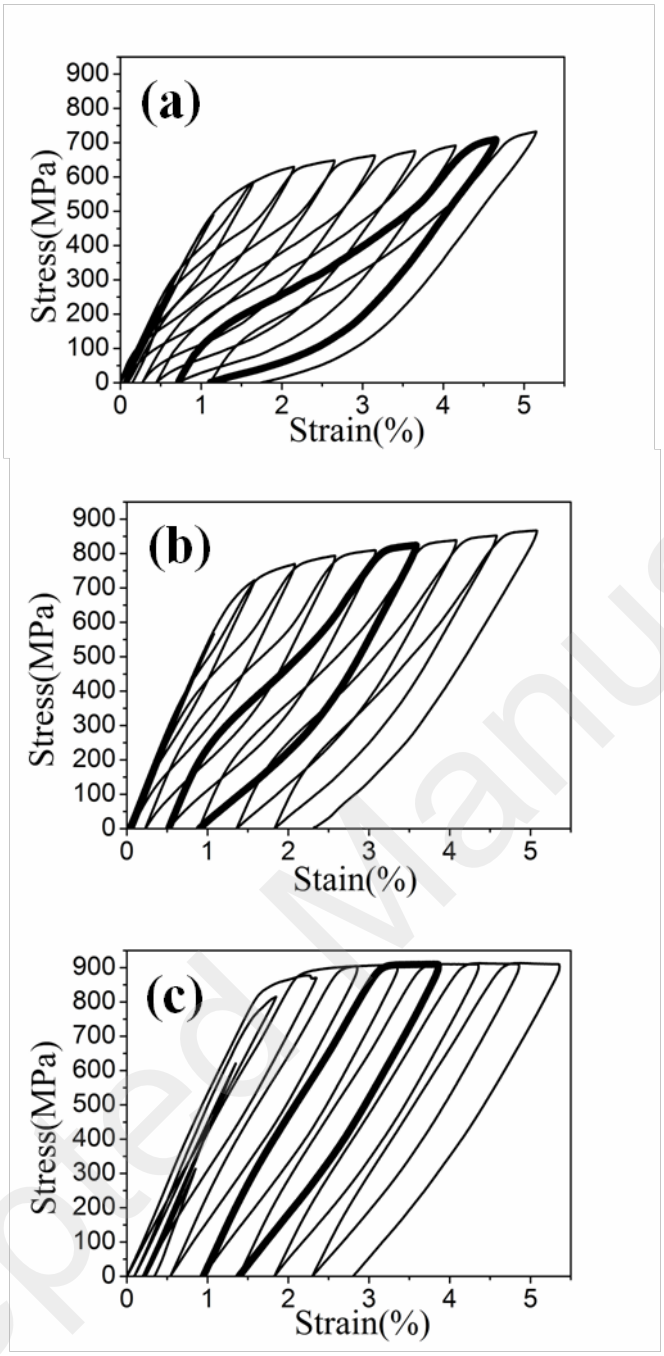

Fig. 2. Engineering stress-strain curves of the Ti-20Zr-3Mo-3Sn alloy obtained from cyclic tensile tests at room temperature: ST-700-30 (a); ST-800-30 (b); ST-900-30 (c).

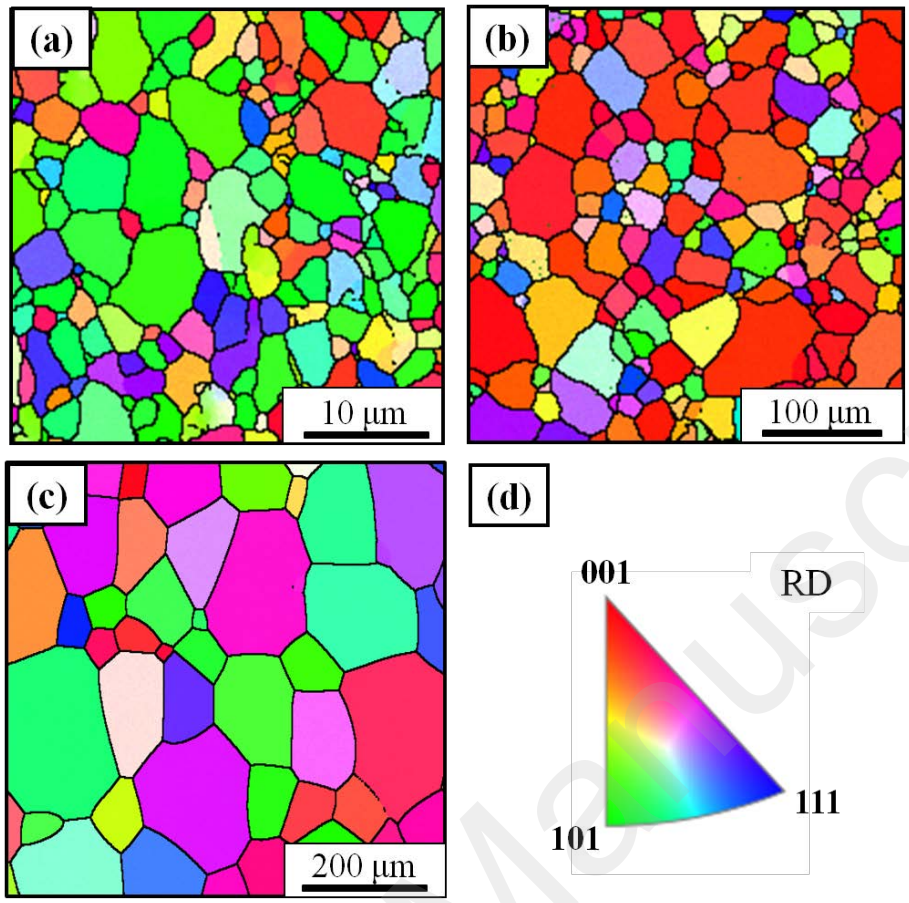

Fig. 3. EBSD RD (Rolling Direction) IPF maps of solution treated alloy samples: ST-700-30 (a); ST-800-30 (b); ST-900-30 (c); IPF color code (d).

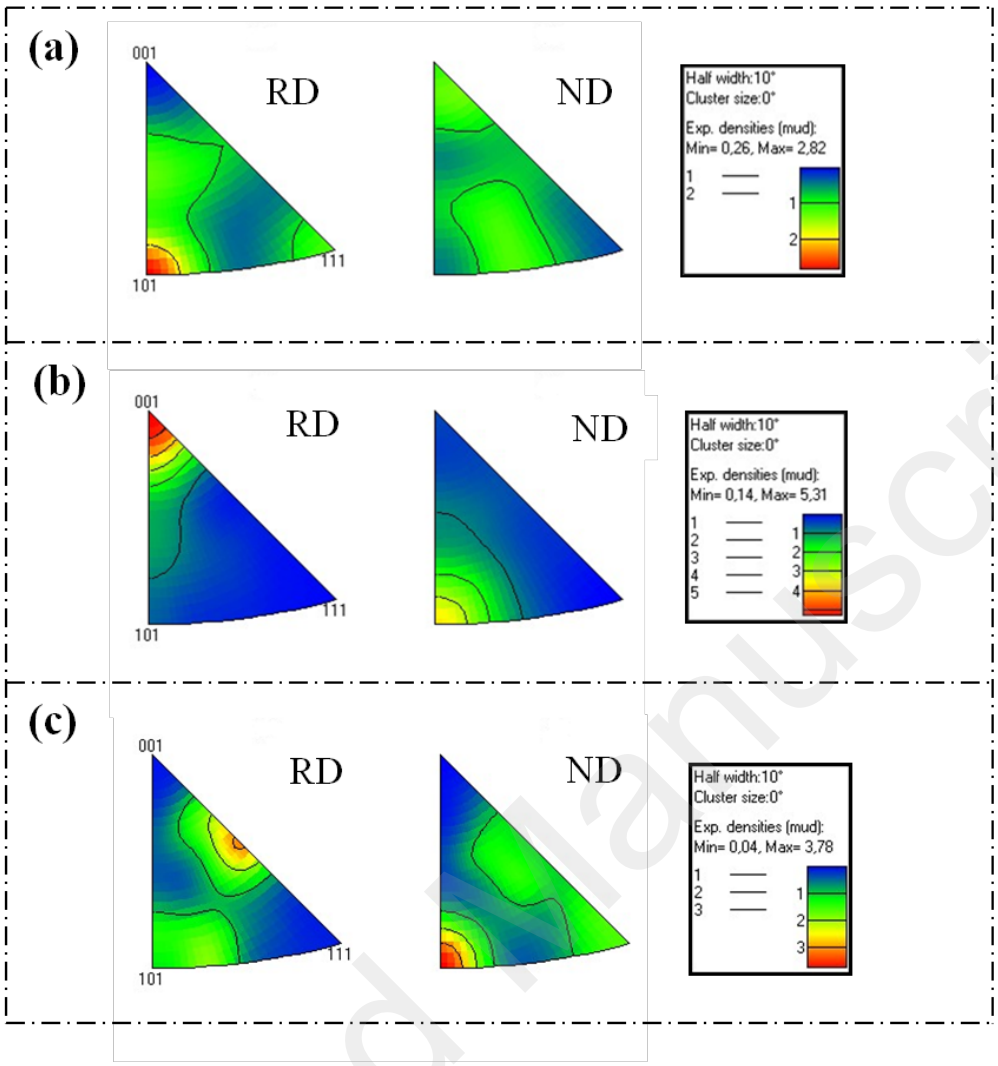

Fig. 4. Inverse pole figures of the solution treated alloy samples: ST-700-30 (a); ST-800-30 (b); ST-900-30 (c). RD is parallel to the tensile direction.

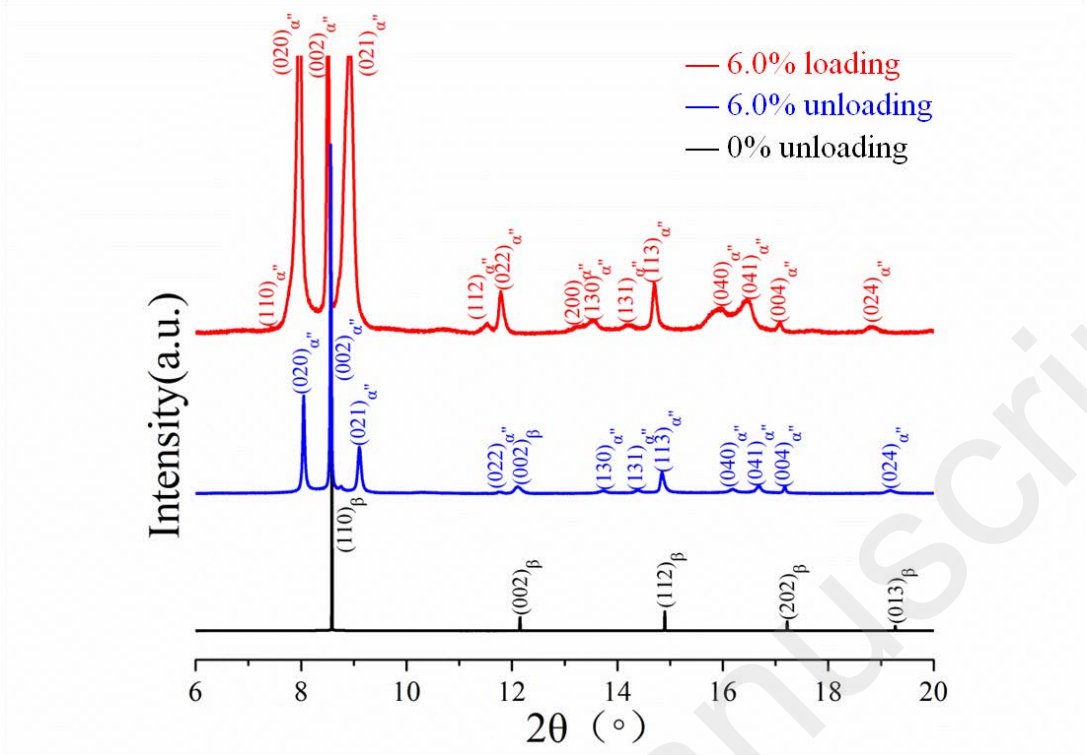

Fig. 5. SXRD profiles for ST-700-30 specimen acquired before deformation (black), under loading at 6.0% of strain (red) and after unloading from 6.0% of strain (blue).

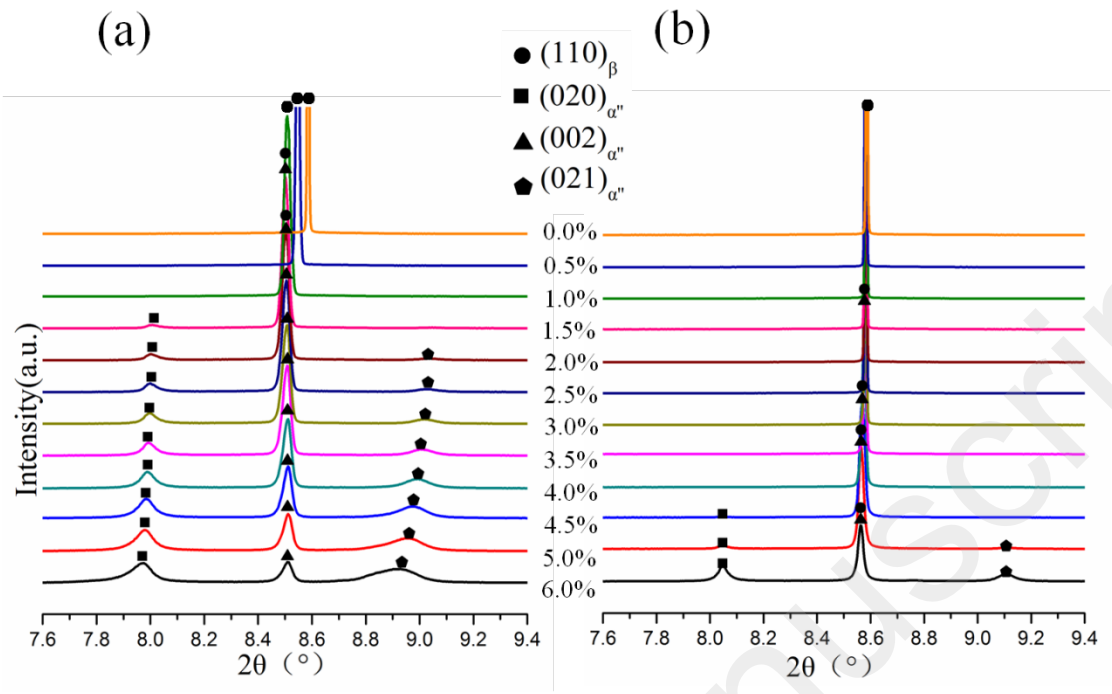

Fig. 6. SXRD profiles zoomed within 2θ=7.6°-9.4° obtained during in situ cyclic tensile test on loading (a) and after unloading (b) for the ST-700-30 specimen.

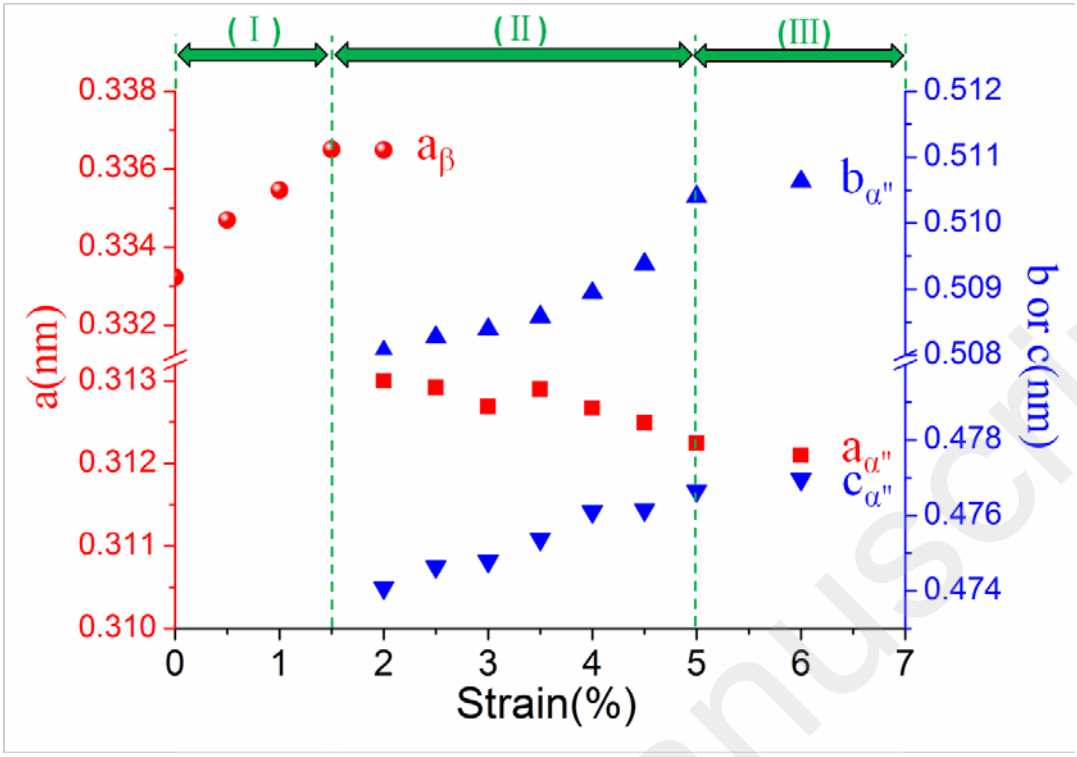

Fig. 7. Evolution of lattice parameters of β and α'' phases as a function of the applied strain for the ST-700-30 sample during in situ cyclic tensile test.

Table 1. Lattice parameters of β and α'' phases, calculated maximum transformation strains in the principal crystallographic directions and measured recovery strains for Ti-20Zr-3Mo-3Sn and Ti-24Nb-4Zr-8Sn alloys.

Alloys	lattice parameter(nm)				ε_{110}	ε_{001}	ε_{111}	recovery strain (%)
	β phase	α'' phase						
	a_β	$a_{\alpha''}$	$b_{\alpha''}$	$c_{\alpha''}$				
Ti20Zr3Mo3Sn	0.336	0.312	0.510	0.477	7.3	3.8	2.5	3.50
Ti24Nb4Zr8Sn[22]	0.333	0.315	0.488	0.484	3.6	3.2	0.6	2.25